

Metadamping enhancement and tunability via scissor-like electromechanical metamaterials

Cite as: J. Appl. Phys. **130**, 184901 (2021); doi: [10.1063/5.0058086](https://doi.org/10.1063/5.0058086)

Submitted: 26 May 2021 · Accepted: 19 October 2021 ·

Published Online: 8 November 2021



Hasan Al Ba'ba'a,  Zhenkun Lin, and Serife Tol^{a)} 

AFFILIATIONS

Department of Mechanical Engineering, University of Michigan, Ann Arbor, Michigan 48109-2125, USA

^{a)}Author to whom correspondence should be addressed: stol@umich.edu

ABSTRACT

We report on a novel scissor-like electromechanical metamaterial (SEMM) with enhanced and tunable damping properties, stemming from its electromechanical resonant effects. The displacement amplification mechanism of the scissor-like structure in SEMM is exploited to amplify the damping ratio for stronger vibration mitigation through the enhanced electrical dissipation of the amplified voltage of the piezoelectric element. The relative dissipation performance, termed as metadamping, is quantified based on complex band structures, which allow frequencies to be complex valued. Using different shunting circuits, the overall damping performance of SEMM is demonstrated to be higher than a statically equivalent traditional systems, such as acoustic metamaterials and monatomic lattices. The dissipation performance of SEMM is numerically verified via finite structure analysis and found to be in an excellent agreement with Bloch's wave analysis. Furthermore, the electromechanical nature of the piezoelectric material in SEMM provides a convenient way to tune the metadamping by adjusting the piezoelectric shunting circuit.

Published under an exclusive license by AIP Publishing. <https://doi.org/10.1063/5.0058086>

I. INTRODUCTION

Metamaterials and phononics crystals (PCs) are novel class of materials architected with structural periodicity. Metamaterials are designed by engineering locally resonating substructures that are on the subwavelength scale, while PCs include periodic lattices modulated with mass or modulus on a scale comparable to the wavelength.¹⁻³ They can exhibit unique properties such as the ability to reduce the wave velocities,⁴ forbid certain frequencies of wave propagation (i.e., bandgaps),^{5,6} and exhibit negative effective mass⁷/ modulus⁸. Hence, both metamaterials and PCs have attracted an increasing research attention for their potential to control acoustic/elastic waves in various applications including vibration mitigation,⁹ wave filtering,¹⁰ focusing,¹¹ energy harvesting,¹² seismic shielding,¹³ etc. In particular, bandgaps offered by periodic structures have been thoroughly investigated as an alternative way to attenuate vibration and noise as compared to using traditional dampers or active vibration control techniques. In order to enable a broadband frequency range of attenuation, researchers have integrated piezoelectric materials in the periodic settings referred to as metastructures.¹⁴⁻¹⁸ Furthermore, inertially amplified mechanisms (i.e., dynamical systems with an artificially heavier mass than its static mass) have been demonstrated to create ultra-

wide bandgaps for vibration suppression at low frequencies.¹⁹⁻²³ Additionally, researchers have investigated dissipative metamaterials (including locally resonating unit cells with viscously damped or viscoelastic elements) for their enhanced damping characteristics so called "metadamping." In contrast to the trade-off in damping and stiffness characteristics of naturally occurring materials, dissipative metamaterials are relatively stiff structures with strong load bearing capacity.²⁴⁻²⁷

In general, the analysis of metamaterials and PCs and their dynamic response are considered for unit cells with non-dissipative material constituents. Researchers describe their dynamic behavior by solving the dispersion equation relating the wave vector of a wave to its frequency via Bloch theorem which can be applied to a single unit cell of the periodic structure and solving the eigenvalue problem. Assuming non-dissipative linear material constituents, the dispersion analysis results in real-valued frequencies and generally complex wave vectors (imaginary part reflects *spatial* wave attenuation). When the unit cell exhibits a dissipative behavior, on the other hand, frequency can be modeled as complex-valued to account for *temporal* wave attenuation²⁴. Researchers have investigated the effect of material losses for both metamaterials and PCs and developed solution techniques considering the dissipative effects.^{24,28-31} Notably, Hussein and

Frazier, using complex dispersion diagrams, revealed that the effect viscous elements in the locally resonating metamaterials can enhance the effective damping ratio (known as metadamping phenomenon).²⁴ The dissipative metamaterials can help with broadening the wave attenuation frequency regime.³² In particular, considering the advances in technology and the need for lightweight materials and stiff structural designs, mechanical and aerospace structures are prone to worse noise, vibration, and harshness (NVH) behavior.³³ As an effective solution for merging lightweight requirements and highly dissipative performance, metadamping can be utilized in NVH applications.

In this paper, we study a new dissipative metamaterial by embedding piezoelectric materials into scissor-like configuration and present a thorough analysis of metadamping toward tunable and enhanced broadband vibration control. To this end, we introduce scissor-like electromechanical metamaterial (SEMM) for tunable and enhanced damping characteristics. Tunability of damping is an important factor in many scenarios, for instance, to provide effective vibration control over a wider range of frequencies.³⁴ Inspired by force-amplified piezoelectric structures^{35,36} and scissor-like metamaterials,³⁷ the proposed periodic design exploits the scissor-like metamaterial concept and the electromechanical nature piezoelectric material, which outperforms metadamping in conventional metamaterials while offering a greater degree of tunability. We utilized the metadamping metric in Ref. 24 to quantify the damping performance based on a generalized complex dispersion relations developed for dissipative structures. Metadamping phenomenon in damped SEMM is shown to be tuned mechanically (via changing the angle of scissor-like structures) and electromechanically (via the piezoelectric shunting circuit) and achieve higher damping capacity in a wide range of design space, relative to equivalent periodic structures, such as acoustic metamaterials (AMs) and monatomic lattices. Unique to our design is the dissipation of energy via an resistive-inductive (or resistive-only) shunting circuit of the piezoelectric element, which is shown to be enhanced if the electromechanical coupling is higher. The damping performance is further aided by the mechanical tunability of the scissor-like structure, which amplifies the voltage output by means of amplified strains of the piezoelectric element. Such damping performance is also assessed when the inertial amplification is present in the system.

This paper is organized as follows: Following the Introduction, Sec. II briefly presents complex dispersion analysis in a damped monatomic lattice (ML). Section III discusses the dynamics and wave characteristics of the proposed SEMM design and theory. The damping performance of SEMM is then compared to classical AM and ML systems, when resistive-inductive and short circuits are used, respectively. The dispersion relation predictions are also verified via analyzing the eigenmodes of the finite structure. Also, the special case of SEMM with resistive shunting circuits is presented. Finally, Sec. IV summarize the key points in this study.

II. COMPLEX DISPERSION ANALYSIS: AN OVERVIEW

A. Mathematical formulation

First, we briefly introduce the mathematical formulation described in Refs. 25 and 38 to obtain the dispersion relation for

complex band structure analysis. In general, the equations of motion for a unit cell can be expressed, in the matrix form, as

$$\mathbf{M}\ddot{\mathbf{z}} + \mathbf{C}\dot{\mathbf{z}} + \mathbf{K}\mathbf{z} = \mathbf{0}, \quad (1)$$

where \mathbf{M} , \mathbf{C} , and \mathbf{K} are the mass, damping, and stiffness matrices, respectively, and \mathbf{z} is the degrees of freedom describing the motion of a unit cell. By virtue of the periodicity, a transformation matrix $\mathbf{T}(\kappa)$ can be defined based on the Bloch theorem, which is a function of a non-dimensional wavenumber κ . Hence, the unit cell degrees of freedom can be condensed to the essential degrees of freedom \mathbf{z}_c using $\mathbf{z} = \mathbf{T}\mathbf{z}_c$, which results in

$$\mathbf{M}_c\ddot{\mathbf{z}}_c + \mathbf{C}_c\dot{\mathbf{z}}_c + \mathbf{K}_c\mathbf{z}_c = \mathbf{0}, \quad (2)$$

where $\mathbf{M}_c(\kappa) = \mathbf{T}^H\mathbf{M}\mathbf{T}$, $\mathbf{C}_c(\kappa) = \mathbf{T}^H\mathbf{C}\mathbf{T}$, and $\mathbf{K}_c(\kappa) = \mathbf{T}^H\mathbf{K}\mathbf{T}$, and the superscript H denotes the Hermitian transpose. To obtain the complex dispersion relations, we assume a solution for the essential degrees of the form $\mathbf{z}_c = \hat{\mathbf{z}}_c e^{i\lambda t}$ and the equation of motion reduces to

$$\mathbf{D}_c\hat{\mathbf{z}}_c = \mathbf{0}, \quad (3)$$

where $\mathbf{D}_c(\kappa, \lambda) = \mathbf{M}_c(\kappa)\lambda^2 + \mathbf{C}_c(\kappa)\lambda + \mathbf{K}_c(\kappa)$ is the dynamic stiffness matrix, λ is a complex-frequency variable, and $\hat{\mathbf{z}}_c$ is a complex amplitude. The eigenvalues λ can be computed by reformulating the equations into a state-space formulation to obtain a linear eigenvalue problem. Alternatively, the determinant of $\mathbf{D}_c(\kappa, \lambda)$ can be derived to obtain the characteristic polynomial (equivalently the dispersion relation) of the system, and the roots of the resulting polynomial yields the eigenvalues λ . Finally, the eigenvalues λ can be generally expressed in the following form:

$$\lambda = -\zeta_s\omega_n \pm i\omega_d; \quad \omega_d = \omega_n\sqrt{1 - \zeta_s^2}, \quad (4)$$

where ω_d is the damped frequency, ζ_s is the damping ratio, and ω_n is the resonant frequency.

B. Monatomic lattice

In this section, we use a dissipative monatomic lattice as an example to illustrate the concept of the complex dispersion relations. A unit cell of an infinitely long chain of a viscously damped monatomic lattice [Fig. 1(a)] is governed by Eq. (1) with the displacement vector $\mathbf{z} = \{u_{i-1} \ u_i\}^T$ and the following matrices:

$$\mathbf{M} = \begin{bmatrix} 0 & 0 \\ 0 & m \end{bmatrix}; \quad \mathbf{C} = c \begin{bmatrix} 1 & -1 \\ -1 & 1 \end{bmatrix}; \quad \mathbf{K} = k \begin{bmatrix} 1 & -1 \\ -1 & 1 \end{bmatrix}, \quad (5)$$

where u_i is the displacement of the i th unit, while m , c , and k are the mass, damping coefficient, and spring constant, respectively. Choosing $\mathbf{z}_c = u_i$, the displacements of the $(i-1)$ th and i th unit cells can be related using the Bloch theorem as $u_{i-1} = u_i e^{-i\kappa}$ (i is the imaginary unit), and, hence, resulting in the transformation

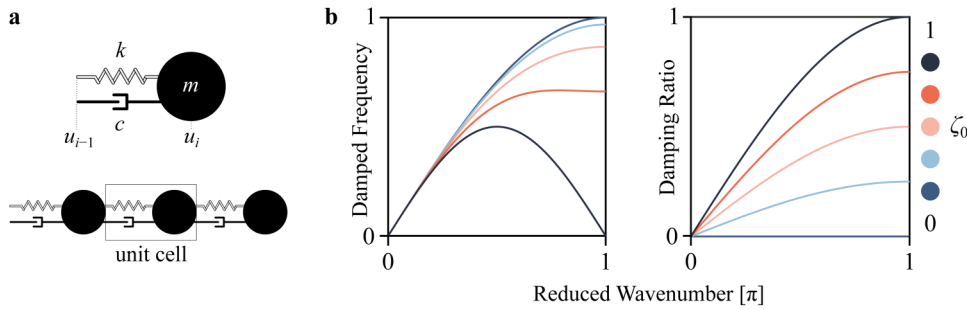


FIG. 1. (a) Schematics of a dissipative monatomic lattice and its unit cell definition. (b) Complex dispersion relations for the monatomic lattice, constituting the damped frequency (left) and corresponding damping ratio (right), under different damping conditions.

$$\mathbf{T} = \begin{bmatrix} e^{-ik} \\ 1 \end{bmatrix}. \tag{6}$$

Following the methodology in Sec. II A, the complex-frequency dispersion relation for the dissipative monatomic lattice is

$$\lambda^2 + 2\zeta_0\omega_0 \sin^2\left(\frac{\kappa}{2}\right)\lambda + \omega_0^2 \sin^2\left(\frac{\kappa}{2}\right) = 0, \tag{7}$$

where

$$\omega_0 = 2\sqrt{\frac{k}{m}}; \quad \zeta_0 = \frac{2\eta}{\omega_0} \tag{8}$$

and $\eta = c/m$ is defined as the damping intensity.³⁹ The dispersion relation in Eq. (7) can be parametrized as

$$\lambda^2 + 2\zeta_s\omega_n\lambda + \omega_n^2 = 0, \tag{9}$$

with the solutions in Eq. (4) and following parameters:

$$\zeta_s = \zeta_0 \left| \sin\left(\frac{\kappa}{2}\right) \right|, \tag{10a}$$

$$\omega_n = \omega_0 \left| \sin\left(\frac{\kappa}{2}\right) \right|. \tag{10b}$$

Note that ω_n is the dispersion relation of an undamped monatomic lattice. Band diagrams of complex-frequency dispersion relations consist of (1) the damped frequency $\omega_d = \omega_n\sqrt{1 - \zeta_s^2}$ (the imaginary part of λ) and (2) the damping ratio ζ_s (the real part of λ normalized by $-\lambda$), as seen in Fig. 1(b). The damped frequency for the monatomic lattice becomes smaller as the damping quantity increases (reflected by the quantity ζ_0), and the damping effect is more pronounced at larger wavenumbers. The corresponding damping ratios increases as ζ_0 becomes larger, as analytically depicted by the amplitude of the sine function in Eq. (10a).

To assess the overall damping performance, we now compute an averaged damping-performance metric developed by Hussein and Frazier,²⁴ which is based on integrating the damping ratio

quantity as (we here normalize by π),

$$\zeta_{\text{avg}} = \frac{1}{\pi} \int_0^\pi \zeta_s d\kappa \tag{11}$$

which, for the monatomic lattice, can be analytically calculated in closed-form as

$$\zeta_{\text{avg}} = \frac{2}{\pi} \zeta_0. \tag{12}$$

In Fig. 2, we plot ζ_{avg} as a function of the non-dimensional quantity ω_0/η . The choice of the quantity ω_0/η is intended to provide an insight into the amount of prescribed damping in the structure relative to its elastic and inertial properties. For a constant value η , if the system has a higher ω_0 , then the prescribed damping becomes small relative to the elastic and inertial properties, thus yielding smaller damping ratios and ζ_{avg} . Similarly, for a given ω_0 , increasing η results in a higher value of ζ_{avg} (and vice versa) as expected.

III. SCISSOR-LIKE ELECTROMECHANICAL METAMATERIAL (SEMM)

A. Design

Here, we propose a new structural design utilizing piezoelectric materials (with resonant shunting circuit) and scissor-like mechanism to exhibit higher metadamping than conventional

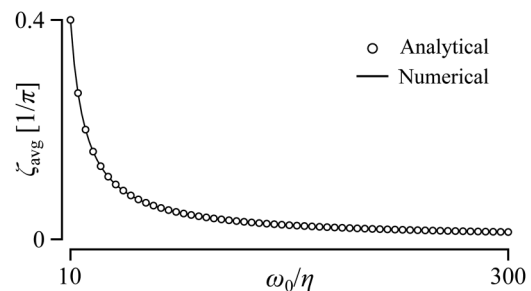


FIG. 2. Averaged damping-performance plot (in units of $1/\pi$) for a monatomic lattice with a swept range of ω_0/η . Circles represent the analytical solution in Eq. (12).

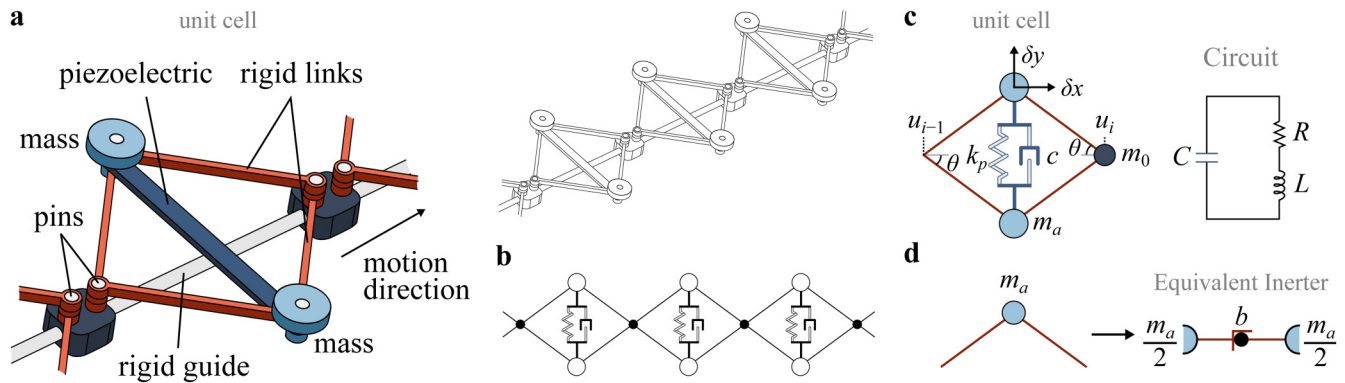


FIG. 3. (a) A physical realization of the proposed SEMM mechanism. (b) Schematics of the SEMM lumped parameter model, consisting of discrete masses m_0 and m_a , massless rigid linkage, and an electromechanical piezoelectric element (modeled as spring k_p and damper c). (c) Unit cell definition of SEMM and its related mechanical and electromechanical properties. (d) Illustrative schematic showing the inertial-amplifier's equivalence to an ideal inerter.⁴⁰

dissipative metamaterials.²⁴ The key mechanism of the proposed SEMM consists of rigid massless linkage with an angle θ , connected via moment-free joints (bearings) as illustrated in Fig. 3(a). Leveraging the shape of the scissor-like configuration, a piezoelectric material (modeled as a spring k_p and a viscous damper c) is configured vertically and its terminals are fixed on the tips of the rigid linkage [Figs. 3(b) and 3(c)]. As a result, a larger mechanical strain can be imposed on the piezoelectric material by virtue of the displacement amplification effects of the scissor-like structure, in response to displacements in the nodes u_i . Such a scissor-like structure has been shown to increase the voltage output in piezoelectric materials.^{35,36} Concentrated masses m_a are located at the top and bottom nodes of the rigid linkage, while masses m_0 are located at the rest of the nodes. The rigid links and tip masses m_a collectively constitutes an inertial amplifier.^{19–22} Owing to the electromechanical coupling in piezoelectric materials, dissipating the mechanical energy in a shunted SEMM can be controlled by the electrical energy generated over the resistive element in the shunting circuit, which can be conveniently tuned to obtain the desired dissipative performance. As such, SEMMs are intended to offer metadamping enhancement (via the amplification mechanisms) with mechanical and electromechanical tunability.

B. Derivations of electromechanically coupled equations of motion

For small vibrational amplitudes, the planar motion of masses m_a in the x - and y -directions are expressed by the joints displacements u_i , such that²¹

$$\delta x = \frac{1}{2}(u_{i-1} + u_i), \tag{13a}$$

$$\delta y = \frac{1}{2} \cot(\theta)(u_{i-1} - u_i). \tag{13b}$$

Next, we express the motion equations of masses m_a in terms of δx and δy and then apply a transformation to represent them in

term of u_{i-1} and u_i and ultimately express them using the degrees of freedom $\mathbf{z}_i^T = \{u_{i-1} \ u_i \ v_i\}$. Both masses m_a collectively move to the right with displacement δx , while the upper (lower) mass moves upward (downward) with a displacement δy_1 (δy_2). Note that the vertical spring only couples the masses in the y -direction. Also, the voltage depends upon the piezoelectric patch's displacement, and in turn, it also affects the vibration response due to the inverse piezoelectric effect. The coupled governing equations of the electromechanical system, assuming a complex frequency, are⁴¹

$$2m_a \lambda^2 \delta x = 0, \tag{14a}$$

$$m_a \delta y_1 \lambda^2 + c(\delta y_1 - \delta y_2) \lambda + k_p(\delta y_1 - \delta y_2) + \vartheta v_i = 0, \tag{14b}$$

$$m_a \delta y_2 \lambda^2 + c(\delta y_2 - \delta y_1) \lambda + k_p(\delta y_2 - \delta y_1) - \vartheta v_i = 0, \tag{14c}$$

$$\left(C\lambda + \frac{1}{Z}\right) v_i + \vartheta(\delta y_2 - \delta y_1) \lambda = 0, \tag{14d}$$

where v_i is the piezoelectric voltage of the i th unit, C is its equivalent capacitance, ϑ is the electromechanical coupling coefficient, and Z is the impedance of the electrical loading of the piezoelectric shunting circuit. Here, the electrical loading impedance is $Z = R + L\lambda$, where R and L are the resistive and inductive loading of the electrical circuit. This choice of electrical loading is intended to induce an electromechanical resonance in the vicinity of the RLC circuit resonance $\omega_R = \sqrt{1/(CL)}$, which introduces a second dispersion branch and opens a locally resonant bandgap similar to the case of mechanical AMs.

Finally, based on the relationship of the displacements δx and $\delta y_{1,2}$ to $u_{i-1,i}$ provided in Eq. (13), a transformation matrix \mathbf{Q} can

be obtained. Hence, we write

$$\begin{Bmatrix} \delta x \\ \delta y_1 \\ \delta y_2 \\ v_i \end{Bmatrix} = \mathbf{Q} \mathbf{z}_i; \quad \mathbf{Q} = \begin{bmatrix} \frac{1}{2} & \frac{1}{2} & 0 \\ \frac{1}{2} \cot(\theta) & -\frac{1}{2} \cot(\theta) & 0 \\ -\frac{1}{2} \cot(\theta) & \frac{1}{2} \cot(\theta) & 0 \\ 0 & 0 & 1 \end{bmatrix}. \quad (15)$$

After post- and pre-multiplying the equations of motion with \mathbf{Q} and \mathbf{Q}^T , respectively, we obtain Eq. (1) with the following effective mass, damping, and stiffness matrices:

$$\mathbf{M} = \begin{bmatrix} m_a + 2b & -2b & 0 \\ -2b & m_0 + m_a + 2b & 0 \\ -\frac{\vartheta}{C} \cot(\theta) & \frac{\vartheta}{C} \cot(\theta) & 1 \end{bmatrix}, \quad (16a)$$

$$\mathbf{C} = \begin{bmatrix} c \cot^2(\theta) & -c \cot^2(\theta) & 0 \\ -c \cot^2(\theta) & c \cot^2(\theta) & 0 \\ -\frac{2\vartheta}{C} \cot(\theta) \zeta_p \omega_R & \frac{2\vartheta}{C} \cot(\theta) \zeta_p \omega_R & 2\zeta_p \omega_R \end{bmatrix}, \quad (16b)$$

$$\mathbf{K} = \begin{bmatrix} k_p \cot^2(\theta) & -k_p \cot^2(\theta) & \vartheta \cot(\theta) \\ -k_p \cot^2(\theta) & k_p \cot^2(\theta) & -\vartheta \cot(\theta) \\ 0 & 0 & \omega_R^2 \end{bmatrix}, \quad (16c)$$

where $b = m_a(\cot^2(\theta) - 1)/4$ is the inertial-amplifier's equivalent inertial (acceleration) coupling constant (often referred to as the inertance⁴²) and $\zeta_p = R/(2L\omega_R)$ is the stand-alone damping ratio of the RLC circuit. Note here that the lumped mass m_0 at the u_i node can be added directly to the mass matrix diagonal, given the discrete nature of the considered problem.

Revisiting Eq. (16), two observations can be made from the equations. First, the form of the mass matrix reveals the working mechanism of the scissor-like configuration when masses m_a are added. Essentially, the dynamics of the scissor-like mechanism and masses m_a combination can be mapped to an ideal inerter, with inertance b , and its static mass is equivalently split on the two nodes as depicted in Fig. 3(d) (see Ref. 40 for more details). If $m_a = 0$, then the inertial-amplification effect is neutralized, given that the coupling inertance becomes zero, i.e., $b = 0$. Second, the displacement amplification effect of the scissor-like structure remains intact as can be observed from the term $\cot(\theta)$ that is multiplied by the electromechanical coupling term ϑ in all matrices, regardless of the mass m_a value. Such additional term, i.e., $\cot(\theta)$, amplifies the electromechanical coupling, which, in turn, amplifies the voltage output of the piezoelectric material at smaller angles θ .

C. Dispersion characteristics of SEMM with resistive-inductive loading

In this section, we derive the dispersion relation of SEMM with a piezoelectric shunting circuit of a resistor and an inductor in a series configuration [Fig. 3(c)]. The structural damping c is neglected in this analysis to emphasize the damping tunability via the shunting circuit. We also choose a mass parametrization of $m_a = m(1 - \mu)/4$ and $m_0 = m(1 + \mu)/2$, such that the total mass of a unit cell is m and the value of the contrast parameter $\mu \in [-1, 1]$ dictates the mass distribution on the rigid linkage

nodes. For instance, $\mu = 1$ ($\mu = -1$) renders $m_a = 0$ ($m_0 = 0$) and $m_0 = m$ ($m_a = m/2$). Following the methodology in Sec. II A and introducing

$$\mathbf{T} = \begin{bmatrix} e^{-ik} & 0 \\ 1 & 0 \\ 0 & 1 \end{bmatrix}. \quad (17)$$

A few mathematical manipulation results in the complex-frequency dispersion relation of the SEMM unit cell

$$\lambda^4 + \alpha_3 \lambda^3 + \alpha_2 \lambda^2 + \alpha_1 \lambda + \alpha_0 = 0, \quad (18)$$

such that

$$\alpha_3 = 2\zeta_p \omega_R, \quad (19a)$$

$$\alpha_2 = \omega_p^2 \hat{q}(1 + \gamma) + \omega_R^2, \quad (19b)$$

$$\alpha_1 = 2\zeta_p \omega_R \omega_p^2 \hat{q}(1 + \gamma), \quad (19c)$$

$$\alpha_0 = \omega_p^2 \omega_R^2 \hat{q}, \quad (19d)$$

where $\omega_p = \sqrt{k_p/m}$, $\gamma = \frac{\vartheta^2}{k_p C}$ is a non-dimensional electromechanical coupling variable, and

$$\hat{q} = \frac{4 \cot^2(\theta) \sin^2(\frac{\kappa}{2})}{\cos^2(\frac{\kappa}{2}) + \frac{1 - \mu \cos(2\theta)}{1 - \cos(2\theta)} \sin^2(\frac{\kappa}{2})}. \quad (20)$$

For $\gamma = 3$, $\theta = \pi/3$, $\mu = 0$, and $\omega_p = \omega_R = 1$ rad/s, Fig. 4(a) shows the damped frequency and damping ratio as a function of the non-dimensional wavenumber for an increasing damping ζ_p . As expected, the dispersion diagrams show that the damping ratio becomes higher as the damping intensity increases and, conversely, the damped frequency becomes smaller in both the acoustic (first) and optic (second) branches. Owing to the structural configuration and electromechanical nature of SEMM, the damping ratio output can be further controlled based on the non-dimensional electromechanical coupling γ and the angle θ , while maintaining the prescribed damping unchanged, as observed in Figs. 4(b) and 4(c) ($\zeta_p = 0.5$ is used). Having higher γ , for instance, increases the damping ratios in the acoustic branch, while decreases them in the optic branch. However, the overall sum of damping ratio curves is higher with higher γ (dotted lines in Fig. 4 bottom panels). In contrast, an increase (a decrease) in the angle θ decreases (increases) the damping ratios in the acoustic (optic) branch and the overall sum of damping ratios tend to be higher with smaller angles. In all cases, the damping ratio for the acoustic branch is overall higher than that of the optic branch, implying that energy can be dissipated at a larger rate for relatively lower frequencies.

D. Metadamping analysis

In this section, we compare the dissipative performance of SEMM to more traditional systems, such as ML and AM. To

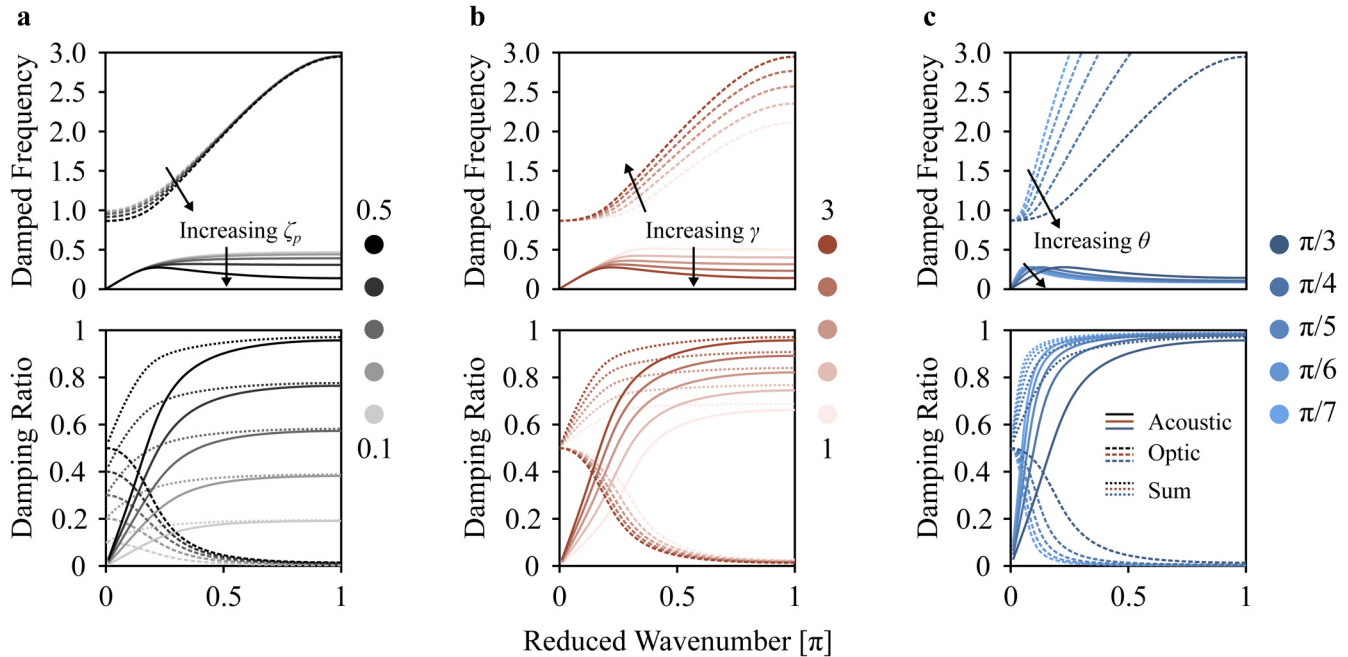


FIG. 4. Complex dispersion relations of SEMM, showing the damped frequency (top) and the corresponding damping ratio (bottom) with varying (a) damping ζ_p , (b) non-dimensional electromechanical coupling γ and (c) amplifier's angle θ .

provide a fair comparison between the different periodic structures, it is essential to have all considered systems exhibiting equivalent (i) static mass and effective stiffness (ensured via an identical sonic speed, i.e., initial slope of the dispersion relation), (ii) damping intensity, and (iii) number of degrees of freedom per unit cell.^{24,25} In what follows are two examples of SEMM with different shunting circuits to demonstrate its capability in increasing damping performance.

1. SEMM with short circuit

We first investigate the SEMM dissipative properties when the piezoelectric material is short circuited, rendering the voltage equal to zero ($v_i = 0$). As such, the mass, damping, and stiffness matrices in Eq. (16) reduce to 2×2 matrices after eliminating the columns and rows pertaining to the voltage variable v_i . Hence, SEMM effectively becomes a variant of the monatomic lattice, which we refer to here as equivalent monatomic lattice (EML) to distinguish from the traditional monatomic lattice. Therefore, it is of interest to compare EML dissipative performance to the traditional monatomic lattice in Fig. 1. In such a case, and with identical damping intensity $\eta = c/m$ and static mass m , it can be shown that the resulting dispersion relation of EML is given by

$$\lambda^2 + \eta \hat{q} \lambda + \omega_p^2 \hat{q} = 0, \tag{21}$$

which is similar to that of ML in Eq. (7). However, EML and ML exhibit different sonic speeds and can be analytically obtained as

$$c_0^{\text{ML}} = \frac{a}{2} \omega_0, \tag{22a}$$

$$c_0^{\text{EML}} = a \omega_p \cot(\theta), \tag{22b}$$

meaning that the condition $\omega_0 = 2\omega_p \cot(\theta)$ must be satisfied to ensure static equivalence (with identical lattice constant a).

For $\omega_p/\eta = 2$ and $\theta = \pi/5$, Figs. 5(a) and 5(b) show the complex dispersion diagram with the damped frequency (normalized in terms of ω_p) and damping ratio. It is seen that EML exhibits higher damping ratios relative to ML, which carries on for a wide range of ω_p/η values, as reflected by ζ_{avg} calculations in Fig. 5(c). This improvement is dependent on the choice of system parameters, which may be hindered at selective parameter ranges. To show such dependence, we calculate the relative damping performance, or metadamping, of EML and ML by introducing the metric²⁴

$$\mathbf{Z} = \zeta_{\text{avg}}^{\text{EML}} - \zeta_{\text{avg}}^{\text{ML}}, \tag{23}$$

which quantifies the difference between the averaged damping ratio of the EML to traditional ML. As shown in the metadamping contour map in Fig. 5(d), smaller angles θ and a larger positive μ generally improve the dissipation performance, indicated by the positive \mathbf{Z} values (i.e., $\zeta_{\text{avg}}^{\text{EML}} > \zeta_{\text{avg}}^{\text{ML}}$). More interestingly, the case of $\mu = 1$ (no inertial amplification effects), in combination of smaller θ , achieve the highest values of \mathbf{Z} . This may be explained in light of the inertial amplification effects from mass m_a . The larger artificial

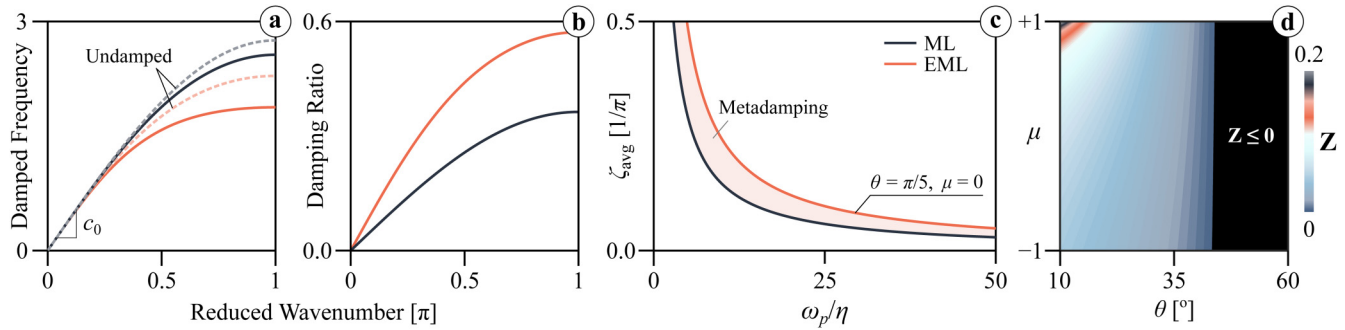


FIG. 5. Complex dispersion relations for EML and ML, constituting the damped frequency (a) and corresponding damping ratio (b). In subfigure (a), the undamped dispersion relations are provided for reference. (c) Averaged damping plot for EML and ML as a function of various values of the resonant frequency relative to the damping intensity, i.e., ω_p/η , demonstrating the metadamping phenomenon (shaded region). (d) Metadamping contour Z for a swept range of parameters μ and θ .

masses on the nodes due inertial amplification may hinder the motion of the nodes and, thus, yielding an overall smaller displacements δy , and, consequently, smaller force on the damping element. It is important to note that large angles θ , typically greater than 45° , also deteriorates the dissipative performance (indicated by the negative Z) as it results in $\cot(\theta) < 1$, meaning that the force is rather reduced in the damper element.

2. SEMM with resistive-inductive circuit

Next, we investigate the damping performance of a resonant SEMM relative to a statically equivalent AM, as shown in Fig. 6. The static mass and damping equivalence of the structure are ensured by setting the total mass of AM to be $m_1 + m_2 = m$ ($m_1 = m_2 = m/2$) and a damping intensity of $\eta = c_2/m_2 = R/L$. That is, the damping in AM is concentrated in its resonator (i.e., $c_1 = 0$ and $c_2 = c$) to be comparable to the SEMM case (where the damping is only in the resonant electrical circuit with neglected structural damping). Finally, and assuming identical lattice

constant a for all systems, the analytical sonic speeds for AM and SEMM, respectively, are derived as

$$c_0^{AM} = \frac{a\omega_1}{\sqrt{2}}; \quad c_0^{SEMM} = a\omega_p \cot(\theta), \quad (24)$$

implying that the following condition has to be satisfied to ensure the static equivalence:

$$\omega_1 = \sqrt{2}\omega_p \cot(\theta); \quad \omega_{1,2} = \sqrt{2k_{1,2}/m}. \quad (25)$$

To satisfy the sonic speed equivalence for any combination of system parameters, we embed the condition for equivalent sonic speed [Eq. (25)] into the dispersion relation of the AM system. For both systems, the dispersion relation can be generally expressed using Eq. (18), albeit with different α coefficients. To facilitate this process, the local resonant frequencies of AM and SEMM are assumed identical, meaning that $\omega_2 = \omega_R$. As a result, a stiffness ratio parameter can be defined as $r_k = \omega_p^2/\omega_R^2 = k_p/(2k_2)$. This procedure is also intended to define an equivalent stiffness ratio for the SEMM case, which is normally challenging given its structural configuration and electromechanical nature. After normalizing with ω_R , the resulting dispersion coefficients are tabulated in Table I.

To compare the dissipation performance, we enforce equivalent prescribed damping amount for all systems, which is reflected by the equivalent value of $\zeta = \eta/(2\omega_R)$ in Table I. Figure 7 shows examples of the complex band structure for AM and SEMM with $r_k = 1$, $\zeta = 0.5$ and, for SEMM only, $\mu = 0$, $\gamma = 3$, and $\theta = \pi/5$.

TABLE I. Coefficients of the dispersion relation for the different lattice structures (i.e., AM and SEMM) with equivalent sonic speed. Note that $\alpha_4 = 1$ for both cases and \bar{q} is defined as $\bar{q} = 4 \sin^2(\kappa/2)$.

Type	α_3	α_2	α_1	α_0
AM	4ζ	$2 + 2r_k \cot^2(\theta)\bar{q}$	$4\zeta r_k \cot^2(\theta)\bar{q}$	$2r_k \cot^2(\theta)\bar{q}$
SEMM	2ζ	$r_k(1 + \gamma)\bar{q} + 1$	$2\zeta r_k(1 + \gamma)\bar{q}$	$r_k\bar{q}$

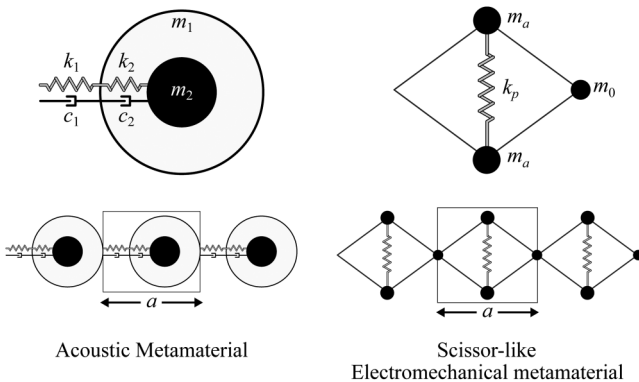


FIG. 6. Schematics of the acoustic metamaterial (AM) and scissor-like electro-mechanical metamaterial (SEMM).

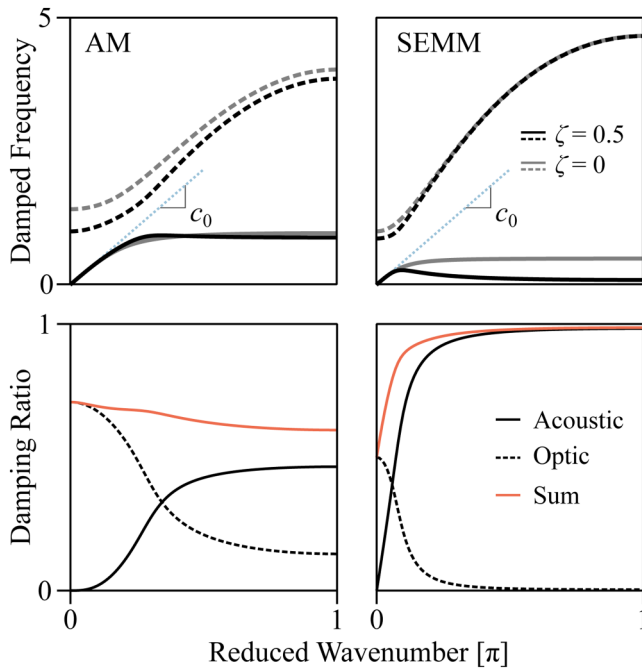


FIG. 7. Comparison of the complex dispersion relations for ML, AM, and SEMM, showing the damped frequencies (top) and their corresponding damping ratio (bottom). Note here that the damped frequency is normalized based on the resonant frequency ω_R .

As can be seen, all dispersion relations have equivalent initial sonic speeds and SEMM has collectively higher damping ratios. This is evident from the sum of the damping ratio curves corresponding to the acoustic and optic modes.

Next, we show the metadamping phenomenon in Fig. 8(a) based on integrating the averaged damping ratios of the acoustic and optic branches as a function of the wavenumber [Eq. (11)] for a swept range of resonant frequencies relative to the damping intensity $\omega_R/\eta \equiv 1/(2\zeta)$. The results reveal that SEMM has a larger damping performance relative to AM, as indicated by the higher values of ζ_{avg} . This result, in fact, varies based on the design parameters (r_k , γ , μ , and θ). To shed light on their effect using the metadamping metric Z , we show the metadamping contours for a swept range of r_k , γ , and μ vs the angle θ , while maintaining the other variables constants (ζ is chosen as 0.05 in all cases). As seen in Fig. 8(b), the metadamping Z increases with the increase in the non-dimensional electromechanical coupling γ (with $\mu = 0$ and $r_k = 1$). Similar improvement is also observed for increasing stiffness ratio r_k [Fig. 8(c) with $\gamma = 3$ and $\mu = 0$]. Last, moving toward positive contrast parameter, μ yields a rather subtle improvement in metadamping, which is more noticeable at smaller angles [Fig. 8(d) with $\gamma = 3$ and $r_k = 1$]. In all three cases, meanwhile, smaller angles θ tend to increase the metadamping performance. The enhancements from decreasing θ and increasing γ can be attributed to the increased voltage output in the electrical circuit from amplified displacement on the piezoelectric and stronger coupling between the

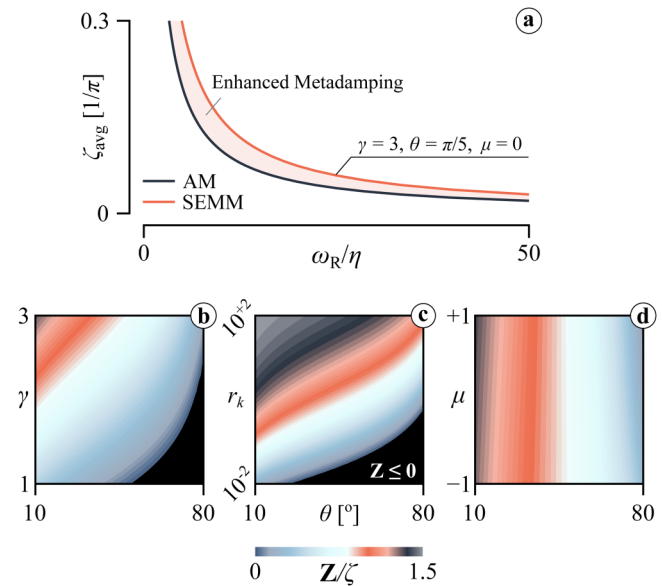


FIG. 8. (a) Averaged damping-performance metric ζ_{avg} as a function of various values of the resonant frequency relative to the damping intensity, i.e., ω_{AM}/η , showing the enhanced metadamping region. (b)–(d) Parametric sweep of the metadamping metric Z for a swept range of the amplification angle θ and (b) non-dimensional electromechanical coupling coefficient γ , (c) stiffness ratio r_k and (d) the contrast parameter μ .

mechanical and electromechanical domains, respectively. As a consequence, SEMM is capable of dissipating more energy in the electrical circuit due the elevated voltage outputs.

E. Complex dispersion validation via a finite system

To verify the theoretical predictions of the complex dispersion relations presented earlier, we simulate a finite lattice of each lattice type with a fixed-free boundary condition and 10 unit cells. In general, the equation of motion for a dissipative dynamical system can be expressed in a state-space formulation as

$$\dot{\mathbf{x}} = \mathbf{A}\mathbf{x} + \mathbf{B}; \quad \mathbf{A} = \begin{bmatrix} \mathbf{0} & \mathbf{I} \\ -\mathbf{M}^{-1}\mathbf{K} & -\mathbf{M}^{-1}\mathbf{C} \end{bmatrix}; \quad (26)$$

$$\mathbf{B} = \begin{bmatrix} \mathbf{0} \\ \mathbf{M}^{-1}\mathbf{f} \end{bmatrix}$$

where $\mathbf{x} = \{\mathbf{z} \dot{\mathbf{z}}\}^T$ and \mathbf{f} are the state and forcing vectors, respectively. For a free-vibration problem and assuming $\mathbf{x} = \hat{\mathbf{x}}e^{\lambda t}$, the state-space equation becomes an eigenvalue problem of the form $\mathbf{A}\hat{\mathbf{x}} = \lambda\hat{\mathbf{x}}$. As a result, we can compute the generally complex eigenvalues λ , and its corresponding damping ratio and damped frequency can be calculated in a similar manner to that of the complex dispersion relation given in Eq. (4). Then, we project the complex modes from the finite structure to a dispersion diagram consisting of the damped frequency and its corresponding damping

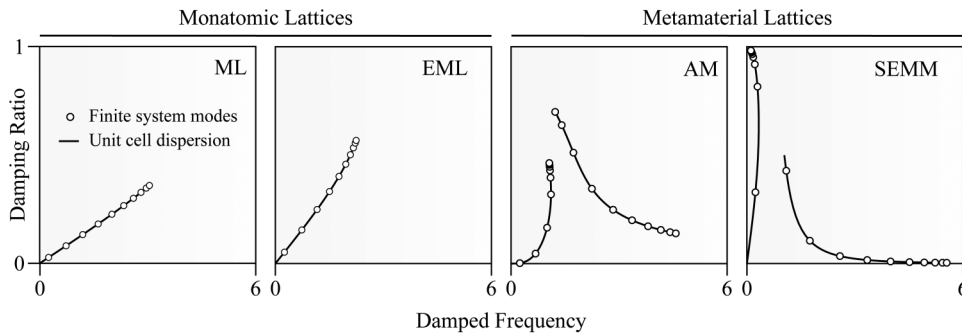


FIG. 9. Comparison between the damped frequency and corresponding damping ratio computed from the finite structure modes and the unit cell dispersion relation, for monatomic lattices (ML and EML) and metamaterial lattices (AM and SEMM).

ratio, a validation method that has been suggested by Aladwani and Nouh.⁴³ As shown in Fig. 9, an excellent agreement is observed between the theoretical unit cell analysis and the finite structure analysis.

F. A special case: SEMM with resistive loading

In this section, we investigate a special case of the shunting circuit of the piezoelectric element, which assumes resistive-only electric loading. Following a similar procedure provided in Sec. III C and assuming $\mu = 1$, the dispersion relation of SEMM with resistive loading can be obtained

$$\lambda^3 + \frac{1}{\tau_c} \lambda^2 + (1 + \gamma) \omega_p^2 \cot^2(\theta) \bar{q} \lambda + \frac{\omega_p^2}{\tau_c} \cot^2(\theta) \bar{q} = 0, \quad (27)$$

where $\bar{q} = 4 \sin^2(\kappa/2)$ and $\tau_c = RC$ is the RC circuit time constant. Of specific interest here is to see the system damping performance as the piezoelectric shunting circuit transition from the short circuit ($R \rightarrow 0$) to the open circuit states ($R \rightarrow \infty$). In both cases, we get a dispersion relation reminiscent to that of an undamped monatomic lattice, albeit with a different cut-off frequency and sonic speeds, owing to the stiffening of piezoelectric as the circuit transitions to open state. The dispersion relation for the short circuit condition becomes

$$\omega = 2\omega_p \cot(\theta) \left| \sin\left(\frac{\kappa}{2}\right) \right|, \quad (28)$$

while the open circuit counterpart is

$$\omega = 2\omega_p \sqrt{1 + \gamma \cot(\theta)} \left| \sin\left(\frac{\kappa}{2}\right) \right|. \quad (29)$$

Evaluating the derivative of the dispersion relation results in the following formulae for the sonic speeds:

$$c_0^s = a\omega_p \cot(\theta), \quad (30a)$$

$$c_0^o = a\omega_p \sqrt{1 + \gamma \cot(\theta)}, \quad (30b)$$

for the short and open circuit conditions, respectively. Having such transition in the sonic speed with increasing the resistance (the damping in the system) is unique to SEMM with resistive loading,

which may not have an equivalent mechanical system. This hinders the comparison of its dissipative performance relative to other dissipative elastic structures, such as AM and ML.

To observe the transition of the dispersion relation from the open circuit to short circuit configurations, we plot several SEMM dispersion relations with varying time constants, as shown in Figs. 10(a) and 10(b) (for $\omega_p = 1$ rad/s, $\theta = \pi/5$, and $\gamma = 3$). As can be seen, the initial slope of the dispersion relation (i.e., sonic speed) remain nearly the same [at about c_0^s in Eq. (30a)] for small

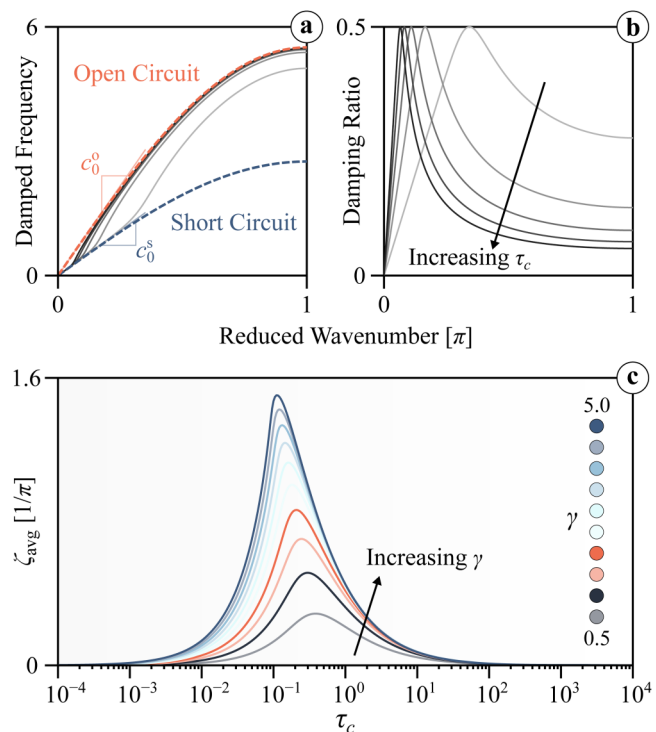


FIG. 10. (a) and (b) Complex dispersion relations and (c) metadamping metric response (with varying electromechanical coupling) for the SEMM system with RC circuit as the circuit transitions from short to open circuit states (i.e., an increasing time constant τ_c).

τ_c . As τ_c becomes larger, the sonic speed eventually transition to a larger value corresponding to the open circuit state, i.e., c_0^o in Eq. (30b). It is also observed that, for some time constant values, the damping ratio has a distinctive peak at a given wavenumber, which shift towards $\kappa = 0$ as τ_c increases.

The averaged damping ζ_{avg} can be computed for a swept values of the time constant τ_c to shed light on the dissipation performance during the transition from short circuit to open circuit states [Fig. 10(c)]. Indeed, the open ($\tau_c \rightarrow \infty$) and short ($\tau_c \rightarrow 0$) circuit conditions render ζ_{avg} nearly equal to zero (effectively undamped), while it peaks at some point during the transition. The location of the peak seems to shift depending on the electromechanical coupling γ and approximately lies midway of the simulated values of $\tau_c \in [10^{-4}, 10^4]$.

IV. CONCLUDING REMARKS

In this paper, we have presented a novel concept of scissor-like electromechanical metamaterial (SEMM) that offers enhanced and tunable metadamping through coupling of electromechanical piezoelectric materials with the scissor-like configuration. We have derived the closed-form solution of the dispersion relation for the proposed structure and compared its damping performance to a statically equivalent acoustic metamaterial (AM) and monatomic lattice (ML) with identical prescribed damping. Based on the metadamping metric, SEMM with resistive-inductive (short) electrical circuit condition exhibits an overall higher damping capacity relative to statically equivalent AM (ML). In addition, metadamping of the SEMM is shown to be tunable via mechanical (i.e., angle θ) and electromechanical (i.e., piezoelectric shunting circuit and coupling coefficient γ) means. We have also shed light on the damping performance of SEMM with resistive-only loading as the piezoelectric shunting circuit transitions from short to open circuit conditions. We envision that the established analytical and numerical frameworks will be useful in broadband vibration mitigation in mechanical and aerospace systems and will pave the way for other types of applications pertaining to wave phenomena.

AUTHOR DECLARATIONS

Conflicts of Interest

The authors have no conflicts to disclose.

DATA AVAILABILITY

The data that support the findings of this study are available from the corresponding author upon reasonable request.

REFERENCES

- G. Ma and P. Sheng, "Acoustic metamaterials: From local resonances to broad horizons," *Sci. Adv.* **2**, e1501595 (2016).
- M. I. Hussein, M. J. Leamy, and M. Ruzzene, "Dynamics of phononic materials and structures: Historical origins, recent progress, and future outlook," *Appl. Mech. Rev.* **66**, 040802 (2014).
- P. A. Deymier, *Acoustic Metamaterials and Phononic Crystals* (Springer Science & Business Media, 2013), Vol. 173.
- J. H. Page, P. Sheng, H. P. Schriemer, I. Jones, X. Jing, and D. A. Weitz, "Group velocity in strongly scattering media," *Science* **271**, 634–637 (1996).
- V. Laude, *Phononic Crystals* (de Gruyter, 2020).
- M. M. Sigalas and E. N. Economou, "Elastic and acoustic wave band structure," *J. Sound Vib.* **158**, 377–382 (1992).
- Z. Liu, X. Zhang, Y. Mao, Y. Zhu, Z. Yang, C. T. Chan, and P. Sheng, "Locally resonant sonic materials," *Science* **289**, 1734–1736 (2000).
- N. Fang, D. Xi, J. Xu, M. Ambati, W. Sritravanich, C. Sun, and X. Zhang, "Ultrasonic metamaterials with negative modulus," *Nat. Mater.* **5**, 452–456 (2006).
- Y. Li, E. Baker, T. Reissman, C. Sun, and W. K. Liu, "Design of mechanical metamaterials for simultaneous vibration isolation and energy harvesting," *Appl. Phys. Lett.* **111**, 251903 (2017).
- G. Trainiti, Y. Xia, J. Marconi, G. Cazzulani, A. Erturk, and M. Ruzzene, "Time-periodic stiffness modulation in elastic metamaterials for selective wave filtering: Theory and experiment," *Phys. Rev. Lett.* **122**, 124301 (2019).
- H. Danawe, G. Okudan, D. Ozevin, and S. Tol, "Conformal gradient-index phononic crystal lens for ultrasonic wave focusing in pipe-like structures," *Appl. Phys. Lett.* **117**, 021906 (2020).
- S. Tol, F. Degertekin, and A. Erturk, "3d-printed phononic crystal lens for elastic wave focusing and energy harvesting," *Additive Manufacturing* **29**, 100780 (2019).
- M. Miniaci, A. Krushynska, F. Bosia, and N. M. Pugno, "Large scale mechanical metamaterials as seismic shields," *New J. Phys.* **18**, 083041 (2016).
- Z. Lin, H. A. Ba'ba'a, and S. Tol, "Piezoelectric metastructures for simultaneous broadband energy harvesting and vibration suppression of traveling waves," *arXiv:2104.00188* (2021).
- G. Hu, L. Tang, and R. Das, "Internally coupled metamaterial beam for simultaneous vibration suppression and low frequency energy harvesting," *J. Appl. Phys.* **123**, 055107 (2018).
- C. Sugino and A. Erturk, "Analysis of multifunctional piezoelectric metastructures for low-frequency bandgap formation and energy harvesting," *J. Phys. D: Appl. Phys.* **51** (2018).
- J. S. Chen, W. J. Su, Y. Cheng, W. C. Li, and C. Y. Lin, "A metamaterial structure capable of wave attenuation and concurrent energy harvesting," *J. Intell. Mater. Syst. Struct.* **30**, 2973–2981 (2019).
- M. Alshaqqa and A. Erturk, "Graded multifunctional piezoelectric metastructures for wideband vibration attenuation and energy harvesting," *Smart Mater. Struct.* **30**, 015029 (2020).
- C. Yilmaz, G. M. Hulbert, and N. Kikuchi, "Phononic band gaps induced by inertial amplification in periodic media," *Phys. Rev. B* **76**, 054309 (2007).
- G. Acar and C. Yilmaz, "Experimental and numerical evidence for the existence of wide and deep phononic gaps induced by inertial amplification in two-dimensional solid structures," *J. Sound Vib.* **332**, 6389–6404 (2013).
- N. M. Frandsen, O. R. Bilal, J. S. Jensen, and M. I. Hussein, "Inertial amplification of continuous structures: Large band gaps from small masses," *J. Appl. Phys.* **119**, 124902 (2016).
- S. Taniker and C. Yilmaz, "Generating ultra wide vibration stop bands by a novel inertial amplification mechanism topology with flexure hinges," *Int. J. Solids Struct.* **106–107**, 129–138 (2017).
- A. Banerjee, S. Adhikari, and M. I. Hussein, "Inertial amplification band-gap generation by coupling a levered mass with a locally resonant mass," *Int. J. Mech. Sci.* **207**, 106630 (2021).
- M. I. Hussein and M. J. Frazier, "Metadamping: An emergent phenomenon in dissipative metamaterials," *J. Sound Vib.* **332**, 4767–4774 (2013).
- C. L. Bacquet, H. Al Ba'ba'a, M. J. Frazier, M. Noh, and M. I. Hussein, "Metadamping: Dissipation emergence in elastic metamaterials," in *Advances in Applied Mechanics*, Vol. 51 (Elsevier, 2018), pp. 115–164.
- D. DePauw, H. Al Ba'ba'a, and M. Noh, "Metadamping and energy dissipation enhancement via hybrid phononic resonators," *Extreme Mech. Lett.* **18**, 36–44 (2018).
- A. Aladwani and M. Noh, "Strategic damping placement in viscoelastic bandgap structures: Dissecting the metadamping phenomenon in multiresonator metamaterials," *J. Appl. Mech.* **88**, 021003 (2021).
- R. P. Moiseyenko and V. Laude, "Material loss influence on the complex band structure and group velocity in phononic crystals," *Phys. Rev. B* **83**, 064301 (2011).

- ²⁹M. I. Hussein and M. J. Frazier, "Damped phononic crystals and acoustic metamaterials," in *Acoustic Metamaterials and Phononic Crystals* (Springer, 2013), pp. 201–215.
- ³⁰J. M. Manimala and C. Sun, "Microstructural design studies for locally dissipative acoustic metamaterials," *J. Appl. Phys.* **115**, 023518 (2014).
- ³¹M. Collet, M. Ouisse, M. Ruzzene, and M. Ichchou, "Floquet–Bloch decomposition for the computation of dispersion of two-dimensional periodic, damped mechanical systems," *Int. J. Solids Struct.* **48**, 2837–2848 (2011).
- ³²Y. Y. Chen, M. V. Barnhart, J. K. Chen, G. K. Hu, C. T. Sun, and G. L. Huang, "Dissipative elastic metamaterials for broadband wave mitigation at subwavelength scale," *Compos. Struct.* **136**, 358–371 (2016).
- ³³L. Van Belle, C. Claeys, E. Deckers, and W. Desmet, "On the impact of damping on the dispersion curves of a locally resonant metamaterial: Modelling and experimental validation," *J. Sound Vib.* **409**, 1–23 (2017).
- ³⁴Y. Liu, H. Matsuhisa, and H. Utsuno, "Semi-active vibration isolation system with variable stiffness and damping control," *J. Sound Vib.* **313**, 16–28 (2008).
- ³⁵Y. Kuang, A. Daniels, and M. Zhu, "A sandwiched piezoelectric transducer with flex end-caps for energy harvesting in large force environments," *J. Phys. D: Appl. Phys.* **50**, 345501 (2017).
- ³⁶Y. Wang, W. Chen, and P. Guzman, "Piezoelectric stack energy harvesting with a force amplification frame: Modeling and experiment," *J. Intell. Mater. Syst. Struct.* **27**, 2324–2332 (2016).
- ³⁷Y. Li and W. Zhou, "Bandgap and vibration transfer characteristics of scissor-like periodic metamaterials," *J. Appl. Phys.* **130**, 025103 (2021).
- ³⁸M. I. Hussein, "Theory of damped Bloch waves in elastic media," *Phys. Rev. B* **80**, 212301 (2009).
- ³⁹M. J. Frazier and M. I. Hussein, "Generalized Bloch's theorem for viscous metamaterials: Dispersion and effective properties based on frequencies and wavenumbers that are simultaneously complex," *C. R. Phys.* **17**, 565–577 (2016).
- ⁴⁰H. Al Ba'ba'a, X. Zhu, and Q. Wang, "Enabling novel dispersion and topological characteristics in mechanical lattices via stable negative inertial coupling," *Proc. R. Soc. A* **477**, 220200820 (2021).
- ⁴¹N. E. Dutoit, B. L. Wardle, and S.-G. Kim, "Design considerations for mems-scale piezoelectric mechanical vibration energy harvesters," *Integr. Ferroelectr.* **71**, 121–160 (2005).
- ⁴²M. C. Smith, "Synthesis of mechanical networks: The inerter," *IEEE Trans. Automat. Control* **47**, 1648–1662 (2002).
- ⁴³A. Aladwani and M. Nouh, "Mechanics of metadamping in flexural dissipative metamaterials: Analysis and design in frequency and time domains," *Int. J. Mech. Sci.* **173**, 105459 (2020).